actuators

MDPI

Article

Dual-Sliding-Surface Robust Control for the PEMFC Air-Feeding System Based on Terminal Sliding Mode Algorithm

Shiyi Fang [1,†], Jianan Feng [1,†], Xinyu Fan [1,*], Daifen Chen [1,*] and Cao Tan [2]

[1] School of Energy and Power, Jiangsu University of Science and Technology, Zhenjiang 212100, China; shiyifang@stu.just.edu.cn (S.F.); jnfeng@stu.just.edu.cn (J.F.)
[2] School of Transport and Vehicle Engineering, Shandong University of Technology, Zibo 255100, China; njusttancao@yeah.net
* Correspondence: fanxy@just.edu.cn (X.F.); dfchen@just.edu.cn (D.C.)
† These authors contributed equally to this work.

Abstract: The proton exchange membrane fuel cell (PEMFC) is the most widely used fuel cell, but it also has some limitations. One of the research pain points is controlling the oxygen content in PEMFCs. A moderate excess of oxygen boosts electrochemical reaction efficiency, while an appropriate oxygen content ensures system stability. In this paper, a fourth-order nonlinear mathematical model of a PEMFC stack air supply system is established to solve the problem of optimal oxygen excess ratio (OER) control under dynamic load conditions. Based on the model, a nonsingular terminal sliding mode controller (NTSMC) based on a sliding mode observer (SMO) is proposed. The NTSM exhibits superior robustness and performance compared to other sliding mode structures. Meanwhile, the SMO accurately predicts system states, facilitating precise control actions. Additionally, the dual sliding mode surfaces enhance system stability against parameter uncertainties and external disturbances. Our results demonstrate that the proposed controller outperforms traditional ones in terms of robustness and performance, which significantly enhances PEMFC system efficiency and stability.

Keywords: PEMFC; oxygen excess ratio (OER); nonsingular terminal sliding mode control; hydrogen energy

check for updates

Citation: Fang, S.; Feng, J.; Fan, X.; Chen, D.; Tan, C. Dual-Sliding-Surface Robust Control for the PEMFC Air-Feeding System Based on Terminal Sliding Mode Algorithm. *Actuators* **2024**, *13*, 459. https://doi.org/10.3390/act13110459

Academic Editor: Ioan Ursu

Received: 13 October 2024
Revised: 5 November 2024
Accepted: 13 November 2024
Published: 15 November 2024

Copyright: © 2024 by the authors. Licensee MDPI, Basel, Switzerland. This article is an open access article distributed under the terms and conditions of the Creative Commons Attribution (CC BY) license (https://creativecommons.org/licenses/by/4.0/).

1. Introduction

According to the *World Energy Outlook* 2023 report of the International Energy Agency (IEA), many important energy transformations should be realized by 2030, including the growth of clean energy, the reduction of fossil fuels, and the improvement of energy efficiency [1,2]. Hydrogen is the most abundant of all elements in the earth, and it yields high combustion efficiency and no pollution. Therefore, hydrogen energy is still one of the main means to solve the greenhouse effect and promote energy transformation [3,4]. Compared with traditional fossil energy, fuel cells have the advantages of low emissions, silent operation, no pollution, and so on. At present, fuel cells are widely used in transportation and power grids [5,6]. Compared with other types of fuel cells, the proton exchange membrane fuel cell (PEMFC) is the most widely used fuel cell type due to its mature technology. The principle is to generate electric energy through the reaction between hydrogen in the battery and oxygen in the air. This kind of electric energy is generated by electrochemical reaction, which is the key to its high level of energy conversion efficiency [7,8].

In our previous research [9], we studied the air distribution characteristics in fuel cell stacks with different channel structures through a large-scale 3D electrochemical and multiphysical field coupling model to further optimize the structures of fuel cells. In addition, we further coupled the electrochemical and multiphysical field models with a thermomechanical model to study the influence of different component structures on the distribution of mechanical stress in the stack. However, the amount of oxygen supplied to the system has a great impact on the performance of a PEMFC stack. Oxygen content

that is either too high or too low will cause irreversible damage to the stack. Therefore, it is necessary to control the cathode supply system through excellent control methods in the face of dynamic and complex conditions [10,11]. At present, air supply control is still a hot and difficult point in the control of PEMFC systems [12,13].

To date, many control strategies have been applied in PEMFC systems. The dynamic adjustment of PID controller parameters through the application of an optimization algorithm is a widely adopted methodology in current practice [14]. In PEMFCs, a hybrid fuzzy PID method [15] and a nonlinear-observer-based PID method [16] have been proposed to control the cathode supply system. Meanwhile, H. Yue has estimated the OER of PEMFCs based on the improved active disturbance rejection control (IADRC) strategy of adaptive unscented Kalman filtering (AUKF) [17]. The simulation results show that the strategy can effectively improve the system responsiveness and robustness to structural parameters. In comparison to classical control, sliding mode control (SMC) presents strong robustness, excellent tracking performance, and heightened system stability [18,19]. Abbaker designed an adaptive sliding mode controller for PEMFC air management systems. The simulation results indicate that the proposed controller is capable of achieving rapid convergence of the tracking trajectory while minimizing fluctuations [20]. Random time gradient adaptive sliding control mode was also proposed to regulate gas control [21]. Especially, a terminal sliding mode structure (TSMC) utilizes a nonlinear sliding surface that facilitates quicker convergence of the system state towards the sliding surface [22,23]. MPC (Model Predict Control) is also simultaneously capable of handling complex systems with multiple inputs and multiple outputs due to its predictive nature. In PEMFCs, Z. Liu proposed an improved MPC strategy for vehicle fuel cell thermal management, which combines model adaptation, the use of forward-looking information, and temperature trajectory planning [24]. D. Yang used fuzzy logic to further optimize MPC controllers of PEMFCs [25]. Wang combined MPC with PID to improve control performance [26]. What's more, intelligent controllers are used in PEMFC by many researchers. J. Li designed an intelligent controller that can adapt to various fuel cell conditions based on deep reinforcement [22]. Neural network and random forest algorithm methods are used to predict system states [11,27], further enhancing the system robustness.

Nevertheless, the above control systems fail to fully address the challenge of achieving optimal control for the PEMFC supply when subjected to variable disturbances. Meanwhile, considering PEMFCs are complex yet SISO (single-input, single-output) systems, NTSMC is more suitable than MPC due to its nonlinear characteristics. Based on these considerations, a terminal sliding mode controller based on a sliding mode observer has been proposed [28,29], adjusting the oxygen excess and preventing hypoxia [23]. The sliding mode observer was used to estimate the uncertain parameters in the air supply system. The dual-sliding mode surfaces proposed by this control method make the system more stable in the face of system parameter uncertainty and external disturbance.

The organization of this study proceeds as follows: Firstly, the mathematical models pertaining to the PEMFC cathode supply system are established. Secondly, an analysis and evaluation of the design process of the control system designed for the PEMFC cathode air management system are undertaken. Finally, the results are rigorously examined, deliberated, and compared with other controllers to establish benchmarks.

2. Four-State PEMFC System Model

A PEMFC system is mainly composed of subsystems such as the supply system, cooling system, thermal management system, etc., as shown in Figure 1. These subsystems work together to complete the energy conversion [30]. To simplify the influence of other factors on the air supply, the hydrodynamic system model is assumed as the following:

(1) All gases follow the ideal gas law.
(2) The PEMFC's thermal subsystem maintains stack temp. at 80 °C.
(3) The PEMFC model is 1D lumped-parameter.
(4) Air's N_2:O_2 ratio is 79:21.

(5) Intake air relative humidity is constant.

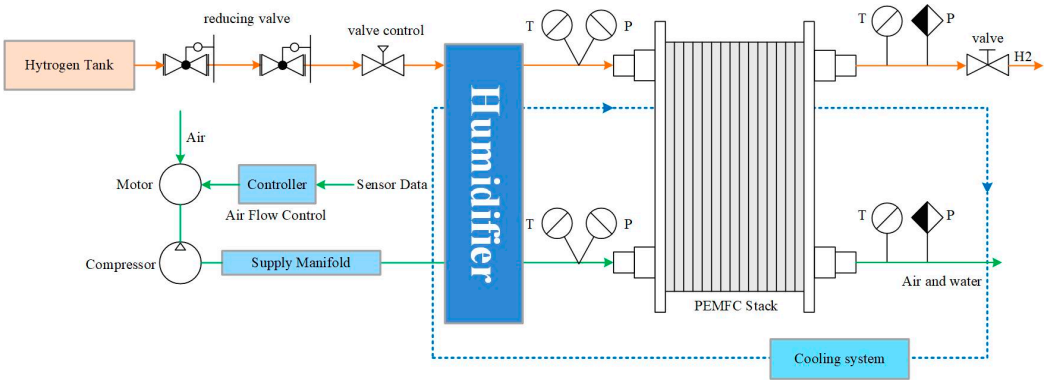


Figure 1. Sketch diagram of a typical PEMFC system.

2.1. PEMFC Voltage Model

During the operation of PEMFCs, it is impossible to avoid activation overpotential, which arises from the sluggish reaction rate within the electrode. A portion of the voltage is expended in the electrochemical reaction. Activation polarization occurs at both the cathode and anode of the PEMFC, and its magnitude can be approximated as

$$V_{act} = -\left[\varepsilon_1 + \varepsilon_2 T_{st} + \varepsilon_3 T_{st} \ln\left(C_{O_2}\right) + \varepsilon_4 T_{st} \ln I_{\mathrm{st}}\right] \tag{1}$$

where ε_1, ε_2, ε_3, and ε_4, are the model coefficients, and I_{st} is the stack electric current [31]. P_{O_2} is the oxygen partial pressure, and C_{O_2} can be calculated by the Herry Theorem ($C_{O_2} = P_{O_2}/[5080000\exp(-498/T_{\mathrm{st}})]$).

The movement of electric charges generates impedance and results in ohmic polarization loss. This voltage loss is fundamentally attributed to the resistance and structural properties of the electrode and electrolyte materials.

$$V_{ohm} = \frac{I_{\mathrm{st}}}{1000} A(R_C + R_M) \tag{2}$$

where R_C and R_M are the equivalent resistances of the electron and proton channels, respectively.

The concentration polarization loss arises from variations in reactant and product concentrations between the reaction sites and inlets. Additionally, the concentration gradient of the species serves as a primary driving force for their transport within the porous electrodes.

$$V_{\mathrm{con}} = m\exp(ni) \tag{3}$$

where n is the empirical value, and m can be evaluated according to Ref. [12].

The thermodynamic theoretical electromotive force represents the theoretical maximum output voltage of a single fuel cell. The Nernst equation serves as a bridge between these two fields, elucidating the quantitative relationship between electrode potential and changes in reactant activity and Gibbs free energy. The Nernst electromotive force of a single PEMFC can be obtained by

$$E_{\mathrm{n}} = 1.229 - a(T_{\mathrm{st}} - 298.15) + bT_{\mathrm{st}}\left[\ln\left(P_{\mathrm{H_2}}\right) + \frac{1}{2}\ln\left(P_{\mathrm{O_2}}\right)\right] \tag{4}$$

where a and b are constant, P_{H2} is the hydrogen partial pressure, and T_{st} is the stack temperature [32].

Then, the actual output voltage V_{C} of a single PEMFC can be expressed as

$$V_{\mathrm{C}} = E_{\mathrm{n}} - V_{\mathrm{act}} - V_{\mathrm{ohm}} - V_{\mathrm{con}}\,. \tag{5}$$

Further, the actual output of a PEMFC unit can be denoted as

$$P_c = V_c I_{st}. \tag{6}$$

2.2. Model Validation

To precisely evaluate the simulation, the PEMFC stack model employed in this study was compared to the experimental investigation of Zhu [28]. The relevant parameters of the simulation model are delineated in Table 1 [15,30]. As illustrated in Figure 2, the outcomes demonstrate a notable congruence between the two studies under identical conditions. It is worth noting that Zhu's experiments were confined to low and medium current densities. Consequently, there might be slight discrepancies at high current densities, attributable to differences in the modeling of concentration voltage losses. Nevertheless, the relative error range in this study remained below 3.3% [33].

Table 1. System-relevant parameters.

Parameter	Description	Value	Unit
η_{Cp}	Motor mechanical efficiency	0.98	%
η_{Cm}	Compressor efficiency	0.80	%
R_{om}	Compressor motor resistance	0.82	Ω
J_{cp}	Compressor inertia	5×10^{-5}	kg m^2
M_v	Vapor molar mass	18×10^{-3}	kg mol^{-1}
$M_{a,atm}$	Air molar mass	29×10^{-3}	kg mol^{-1}
M_{O_2}	Oxygen molar mass	32×10^{-3}	kg mol^{-1}
M_{N_2}	Nitrogen molar mass	28×10^{-3}	kg mol^{-1}
k_v	Motor electric constant	0.0153	V rad^{-1} s
k_t	Motor torque constant	0.0153	(N m)/A
$k_{ca,in}$	Cathode inlet orifice constant	0.36×10^{-5}	kg s^{-1} pa^{-1}
$y_{O_2,atm}$	Oxygen mole fraction	0.21	-
V_{ca}	Cathode volume	0.01	m^3
V_{sm}	Supply manifold volume	0.02	m^3
P_{atm}	Atmospheric pressure	101,325	pa
P_{sat}	Saturation pressure	465,327.41	pa
T_{atm}	Atmospheric temperature	298.15	K
T_{st}	Stack temperature	353.15	K
R	Universal gas constant	8.31	J mol^{-1} K^{-1}
C_D	Cathode outlet throttle discharge coefficient	0.012	-
C_p	Constant pressure specific heat of air	1004	J mol^{-1} K^{-1}
F	Faraday number	96,485	C mol^{-1}
n	Number of cells in fuel cell stack	381	-
A_T	Cathode outlet throttle area	0.002	m^2
γ	Ratio of specific heat of air	1.40	-
ϕ_{atm}	Average ambient air relative humidity	0.50	-

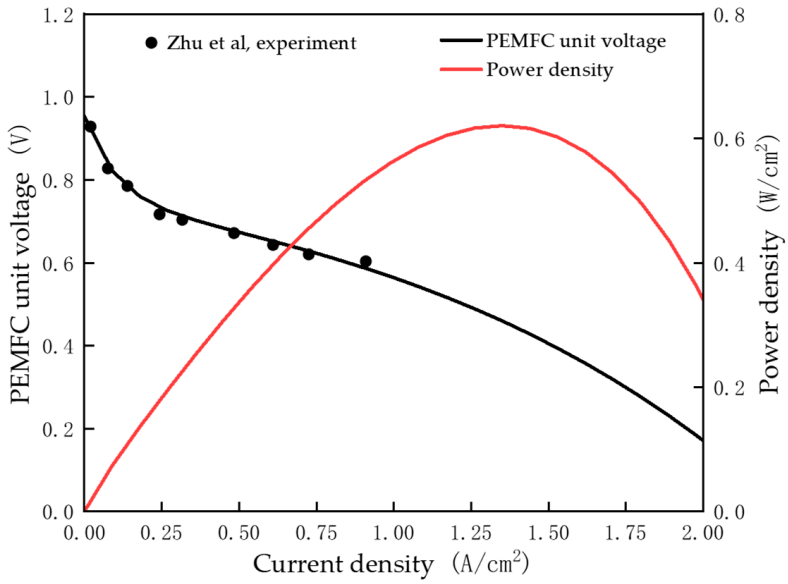


Figure 2. Polarization and power density curves of this research and Zhu's experiment [28].

2.3. Establishment of System State Equations

As shown in Figure 3, the cathode supply system utilizes a motor-driven compressor to compress ambient air. Subsequently, the compressed air is distributed and conveyed through an air supply manifold, ensuring uniform delivery to the cathode section of the PEMFC. In this Figure, n_{motor} represents the motor rotation speed, w_{cp} depicts the air flow rate of the compressor, u denotes the input voltage of the motor, $w_{\text{ca,in}}$ is the air flow rate to the cathode, and P_{sm} and P_{ca} represent the pressure of the supply manifold and cathode, respectively.

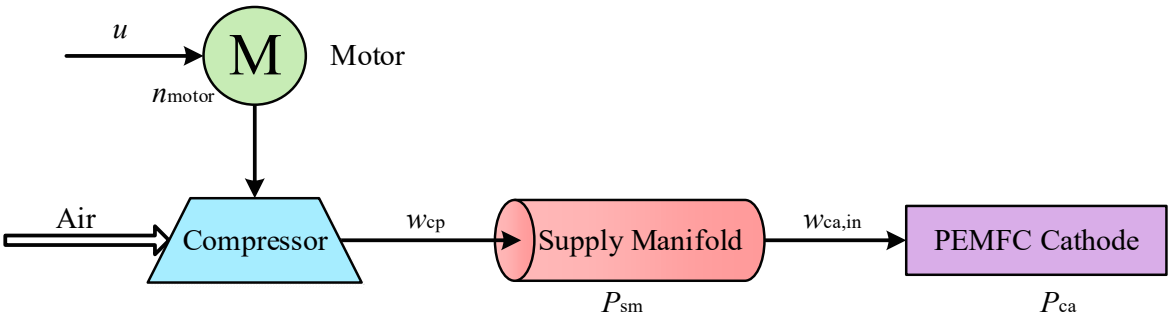


Figure 3. Supply system structure.

The relationship between manifold pressure and airflow is governed by mass conservation. Concurrently, electrochemical reactions induce variations in both the temperature and pressure at the cathode. By utilizing the mass conservation equation alongside the ideal gas equation, a mathematic model for the cathode is established as

$$\begin{cases} \frac{dP_{O_2}}{dt} = \frac{RT_{st}k_{ca,in}}{M_{O_2}V_{ca}}\left(\frac{\chi_{O_2,atm}}{1+\omega_{atm}}\right)(P_{sm} - P_{O_2} - P_{N_2} - P_{\text{sat}}) - \frac{RT_{st}\omega(t)}{V_{ca}}\frac{P_{O_2}}{M_{O_2}P_{O_2}+M_{N_2}P_{N_2}+M_V P_{sat}} - \frac{RT_{st}I_{st}n}{4FV_{ca}} \\ \frac{dP_{N_2}}{dt} = \frac{RT_{st}k_{ca,in}}{M_{N_2}V_{ca}}\left(\frac{1-\chi_{O_2,atm}}{1+\omega_{atm}}\right)(P_{sm} - P_{O_2} - P_{N_2} - P_{\text{sat}}) - \frac{RT_{st}\omega(t)}{V_{ca}}\frac{P_{N_2}}{M_{O_2}P_{O_2}+M_{N_2}P_{N_2}+M_V P_{sat}} - \frac{RT_{st}I_{st}n}{4FV_{ca}} \\ \frac{dn_{motor}}{dt} = -\frac{k_t k_v \eta_{cm}}{R_{cm}J_{cp}}n_{motor} - \left(\left(\frac{P_{sm}}{P_{atm}}\right)^{\frac{\gamma-1}{\gamma}} - 1\right)\frac{1}{n_{motor}}\frac{T_{atm}C_p}{J_{cp}\eta_{cp}}C(t) + \frac{k_t\eta_{cm}}{R_{cm}J_{cp}}u \\ \frac{dP_{sm}}{dt} = \frac{RT_{atm}\gamma}{M_{atm}V_{sm}}\left(1 + \left(\frac{1}{\eta_{cp}}\left(\frac{P_{sm}}{P_{atm}}\right)^{\frac{\gamma-1}{\gamma}} - 1\right)\right)(C(t) - k_{ca,in}(P_{sm} - P_{O_2} - P_{N_2} - P_{\text{sat}}) \end{cases} \tag{7}$$

where P_{O_2} is the cathode oxygen pressure, P_{N_2} is the cathode nitrogen pressure, and other parameters are summarized in Table 1 [26,30]. Further, to minimize computational workload, the fourth-order state equations can be described as

$$\begin{cases} \frac{dx_1}{dt} = a_1(x_4 - x_1 - x_2 - a_2) - \frac{a_3 x_1 \omega(t)}{a_4 x_1 + a_5 x_2 + a_6} - a_7 I_{st} \\ \frac{dx_2}{dt} = a_8(x_4 - x_1 - x_2 - a_2) - \frac{a_3 x_2 \omega(t)}{a_4 x_1 + a_5 x_2 + a_6} - a_7 I_{st} \\ \frac{dx_3}{dt} = -a_9 x_3 - \left(\left(\frac{x_4}{a_{14}}\right)^{a_{12}} - 1\right)C(t)\frac{a_{10}}{x_3} + a_{13}u \\ \frac{dx_4}{dt} = a_{14}\left(1 + \left(a_{15}\left(\frac{x_4}{a_{11}}\right)^{a_{12}} - 1\right)\right)(C(t) - a_{16}(x_4 - x_1 - x_2 - a_2) \end{cases} \tag{8}$$

where a_1 to a_{24} are constant coefficients which are collected in Appendix A [15]. x_1 to x_4 are, respectively, the four state quantities of the system ($\frac{dx}{dt} = f(x, I_{st}) + a_{13}u$), where $x = [x_1, x_2, x_3, x_4]^{\text{T}} = [P_{O2}, P_{N2}, n_{motoer}, P_{sm}]^{\text{T}}$. Meanwhile, the compressor mathematical model [34] can be calculated as

$$C(t) = \frac{C_{\max}}{x_3^{\max}}\left(1 - \exp\left(\frac{-r_0\left(\frac{x_3^2}{r_2}\right) - x_4}{r_1 + \frac{x_3^2}{r_2}x_4^{\min}}\right)\right) \tag{9}$$

where $r_0 = 15$, $r_1 = 105$, $r_2 = 462.25$, ${x_4}^{\min} = 5 \times 10^4$ pa, and $C_{\max} = 0.0975$ kg s^{-1}.

2.4. Control Target

Insufficient oxygen supply will lead to extremely high concentration polarization and oxygen starvation, which will seriously reduce the reliability and life of the PEMFC stack. Meanwhile, oxygen content also affects the PEMFC electrochemical reaction efficiency. Based on these, the oxygen excess ratio (OER) is proposed to describe the excess oxygen content, which is the ratio of the incoming oxygen flow to the oxygen consumed. The OER can depicted as

$$\lambda_{O_2} = \frac{Q_{m,\text{ air,provide}}}{Q_{m,\text{ air}}} = \frac{a_{16}a_{23}(x_4 - (x_1 + x_2) - a_2)}{a_{24}I_{st}}. \tag{10}$$

The OER should be selected according to different operating electric currents to obtain the maximum power output. The value range of the optimal OER is usually set between 2.0 and 2.5. According to Ref. [26] in Figure 4, the fitted reference curve of the OER can be described as

$$\lambda_{O_2,ref} = b_1 I^3_{\text{st}} + b_2 I^2_{\text{st}} + b_3 I_{\text{st}} + b_4 \tag{11}$$

where $b_1 = 5.02 \times 10^{-8}$, $b_2 = -2.87 \times 10^{-5}$, $b_3 = -2.23 \times 10^{-2}$, and $b_4 = 2.503$.

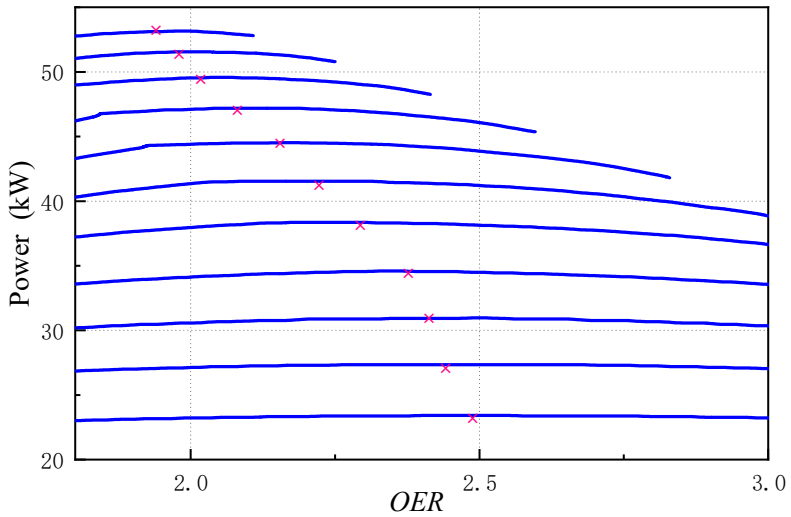


Figure 4. Diagram of power variation with OER under different currents.

To simplify the system calculations, the control objective can be described as

$$z(t) = \frac{a_{24}I_{st}\lambda_{O_2}}{a_{23}}. \tag{12}$$

Based on these, the control error of the system can be defined as

$$\begin{aligned} e_1(t) &= z(t) - z_{ref} \\ &= z(t) - \frac{a_{24}I_{st}\lambda_{O_2,ref}}{a_{23}} \end{aligned}. \tag{13}$$

3. Control System Design

In order to meet the above control requirements, the OER is maintained at its optimal value by an effective controller. In the first part, NTSMC is designed to solve the optimal control law. In the second part, we will propose a sliding mode observer (SMO) for uncertain parameters. Then, a new adaptive double-sliding mode surface structure controller is given, and its structure is shown in Figure 5.

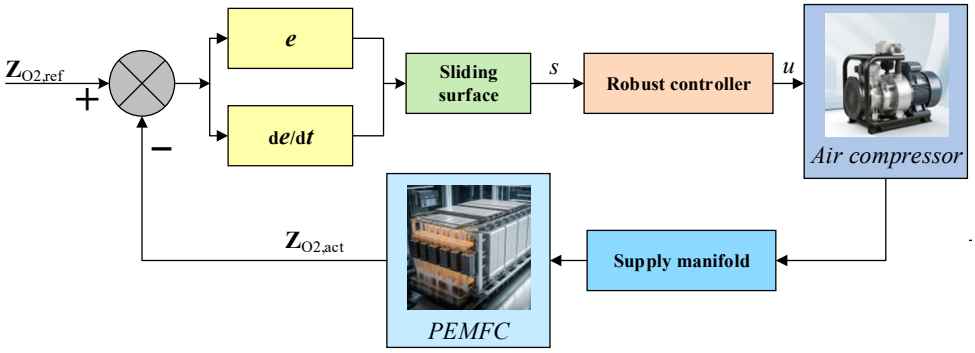


Figure 5. The control block diagram of the system.

3.1. Controller Design

Chattering phenomena are usual in SMC, and a prevalent approach to avoid this issue involves integrating the sliding mode controller with other algorithms [35]. NTSMC optimizes this by redesigning sliding mode structure. Meanwhile, compared to other sliding mode configurations, NTSMC also exhibits superior robustness and performance.

In this section, this new variable structure sliding mode control method is introduced to obtain a fast tracking performance and an accurate tracking effect. As shown in Figure 6, when facing a sudden current change, NTSMC adjusts the air compressor's voltage, guided by sensor data, to achieve the optimal OER for the current, ensuring PEMFC power optimization.

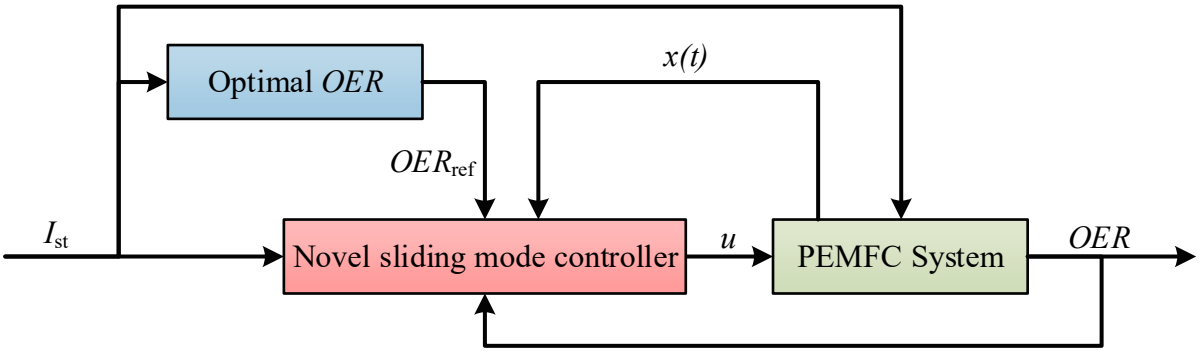


Figure 6. The control block diagram of a single sliding mode controller.

First, select the following fast NTSM surface

$$s = \frac{de_1}{dt} + \kappa_1 e_1 + \kappa_2 g(e_1) \tag{14}$$

where e_1 is the tracking error, e_2 is the first derivative of the tracking error to time, s is the sliding mode variable, k_j (j = 1, 2) is a positive real number, and $g(e_1)$ is

$$g(e_1) = \begin{cases} e_1^{p1/p2} \text{ if ss} = 0 \text{ or ss} \neq 0, |e_1| \geq \mu \\ \gamma_1 e_1 + \gamma_2 sign(e_1) e_1^2 \text{ if ss} \neq 0, |e_1| < \mu \end{cases} \tag{15}$$

where $ss = \frac{de_1}{dt} + \kappa_1 e_1 + \kappa_2 e_1{}^{p_1/p_2}$. μ is a sufficiently small positive number. p_1 and p_2 are the positive odd numbers, and they satisfy $1/2 < p_1/p_2 < 1$. γ_1 and γ_2 are selected as $\gamma_1 = (2 - p_1/p_2)\mu^{p_1/p_2 - 1}$ and $\gamma_2 = (p_1/p_2 - 1)\mu^{p_1/p_2 - 2}$.

The derivative of s can be evaluated as

$$\begin{cases} \frac{ds}{dt} = \frac{d^2 e_1}{dt^2} + \kappa_1 \frac{de_1}{dt} + \kappa_2 \frac{dg(e_1)}{dt} \\ \frac{dg(e_1)}{dt} = \begin{cases} \frac{p_1}{p_2} e_1^{p_1/p_2}, \text{ if ss} = 0 \text{ or ss} \neq 0, |e_1| \geq \mu \\ \gamma_1 \frac{de_1}{dt} + 2\gamma_2 sign(e_1) e_1 \frac{de_1}{dt}, \text{ if ss} \neq 0, |e_1| < \mu \end{cases} \end{cases} \tag{16}$$

The control law is designed as

$$u = u_{eq} + u_{sw} \tag{17}$$

where u_{eq} is the equivalent control and u_{sw} is the switching control. Since there is no lumped disturbance in the internal system, it is not necessary to compensate for lumped disturbance. Thus, $u_{sw} = 0$. If the derivative of the sliding mode variable s is zero, u_{eq} can be inversely solved.

Thus, taking

$$\frac{ds}{dt} = \frac{d^2e_1}{dt^2} + \kappa_1\frac{de_1}{dt} + \kappa_2\frac{dg(e_1)}{dt} = 0 \tag{18}$$

where $\frac{d^2e_1}{dt^2} = \frac{d^2x_4}{dt^2} - (\frac{d^2x_1}{dt^2} + \frac{d^2x_2}{dt^2})$. Here, $\frac{d^2x_4}{dt^2}$ can be described as

$$\frac{d^2x_4}{dt^2} = \frac{dx_1}{dt}\frac{\partial}{\partial x_1}(\frac{dx_4}{dt}) + \frac{dx_2}{dt}\frac{\partial}{\partial x_2}(\frac{dx_4}{dt}) + \frac{dx_3}{dt}\frac{\partial}{\partial x_3}(\frac{dx_4}{dt}) + \frac{dx_4}{dt}\frac{\partial}{\partial x_4}(\frac{dx_4}{dt}) \tag{19}$$

where

$$\begin{cases} \frac{\partial}{\partial x_1}(\frac{dx_4}{dt}) = a_{14}a_{16}(1 + a_{15}((\frac{x_4}{a_{11}})^{a_{12}} - 1)) \\ \frac{\partial}{\partial x_2}(\frac{dx_4}{dt}) = a_{14}a_{16}(1 + a_{15}((\frac{x_4}{a_{11}})^{a_{12}} - 1)) \\ \frac{\partial}{\partial x_3}(\frac{dx_4}{dt}) = a_{14}a_{16}(1 + a_{15}((\frac{x_4}{a_{11}})^{a_{12}} - 1)) \\ \frac{\partial}{\partial x_4}(\frac{dx_4}{dt}) = a_{12}a_{14}a_{15}{a_{11}}^{-a_{12}}(C - a_{16}(x_4 - x_1 - x_2 - a_2)) + a_{14}(1 + a_{15}((\frac{x_4}{a_{11}})^{a_{12}} - 1))(\frac{\partial C}{\partial x_4} - a_{16}) \end{cases}$$

According to Equation (19), we can calculate

$$\frac{d^2x_4}{dt^2} = \frac{dx_1}{dt}\frac{\partial}{\partial x_1}(\frac{dx_4}{dt}) + \frac{dx_2}{dt}\frac{\partial}{\partial x_2}(\frac{dx_4}{dt}) + (-a_9x_3 - ((\frac{x_4}{a_{14}})^{a_{12}} - 1)C(t)\frac{a_{10}}{x_3} + a_{13}u)\frac{\partial}{\partial x_3}(\frac{dx_4}{dt}) + \frac{dx_4}{dt}\frac{\partial}{\partial x_4}(\frac{dx_4}{dt}). \tag{20}$$

Based on Equation (18), $a_{16}(\frac{d^2x_4}{dt^2} - \frac{d^2x_1}{dt^2} - \frac{d^2x_2}{dt^2}) + \kappa_1 a_{16}(\frac{dx_4}{dt} - \frac{dx_1}{dt} - \frac{dx_2}{dt}) + \kappa_2\frac{dg(e_1)}{dt} = 0$ where

$$\begin{cases} \frac{d^2x_1}{dt^2} = (-a_1 + a_3a_4a_{20}\frac{{x_1}^2 + x_1x_2 + a_3x_1}{(a_4x_1 + a_5x_2 + a_6)^2} - a_3a_{20}\frac{2x_1 + x_2 + a_2}{a_4x_1 + a_5x_2 + a_6})\frac{dx_1}{dt} + \\ \qquad (-a_1 + a_3a_5a_{20}\frac{{x_1}^2 + x_1x_2 + a_3x_1}{(a_4x_1 + a_5x_2 + a_6)^2} - \frac{a_3a_{20}x_1}{a_4x_1 + a_5x_2 + a_6})\frac{dx_2}{dt} + a_1\frac{dx_4}{dt} \\ \frac{d^2x_2}{dt^2} = (-a_1 + a_3a_5a_{20}\frac{{x_2}^2 + x_1x_2 + a_3x_2}{(a_4x_1 + a_5x_2 + a_6)^2} - a_3a_{20}\frac{x_1 + 2x_2 + a_2}{a_4x_1 + a_5x_2 + a_6})\frac{dx_2}{dt} + \\ \qquad (-a_1 + a_3a_5a_{20}\frac{{x_2}^2 + x_1x_2 + a_3x_2}{(a_4x_1 + a_5x_2 + a_6)^2} - \frac{a_3a_{20}x_2}{a_4x_1 + a_5x_2 + a_6})\frac{dx_1}{dt} + a_1\frac{dx_4}{dt} \end{cases} \tag{21}$$

Then, u_{eq} can be inversely solved as

$$u_{eq} = \frac{1}{b(x)}(-rsign(s) - is - \mathrm{a}(x)) \tag{22}$$

where r and i are normal numbers, and $a(x)$ and $b(x)$ can be depicted as

$$\begin{cases} a(x) = -a_{16}(\frac{d^2x_1}{dt^2} + \frac{d^2x_2}{dt^2}) + a_{16}(\frac{dx_4}{dt}\frac{\partial}{\partial x_4}(\frac{dx_4}{dt}) + \frac{dx_1}{dt}\frac{\partial}{\partial x_1}(\frac{dx_4}{dt}) + \frac{dx_2}{dt}\frac{\partial}{\partial x_2}(\frac{dx_4}{dt})) \\ \qquad + a_{16}\frac{\partial}{\partial x_3}(\frac{dx_4}{dt})(-a_9x_3 - \frac{a_{10}}{x_3}((\frac{x_4}{a_{14}})^{a_{12}} - 1))C + \kappa_1\frac{dg(e_1)}{dt} \\ \mathrm{b}(x) = a_{13}a_{16}\frac{\partial}{\partial x_3}(\frac{dx_4}{dt}) \end{cases}$$

3.2. Controller Stability Validation

Theorem 1. *The trajectory reference vector* $q_d = (q_{d1}, \ldots, q_{dn})^T$, *its first derivative* $\frac{dq_d}{dt} = (\frac{dq_{d1}}{dt}, \ldots, \frac{dq_{dn}}{dt})^T$, *and its second derivative* $\frac{d^2q_d}{dt^2} = (\frac{d^2q_{d1}}{dt^2}, \ldots, \frac{d^2q_{dn}}{dt^2})^T$ *meet the following conditions:*

$$|q_{di}| \le q_{u1}\ , \left|\frac{dq_{di}}{dt}\right| \le q_{u2}\ , \left|\frac{d^2q_{di}}{dt^2}\right| \le q_{u3}\ (\mathrm{i} = 1,\ \ldots, \mathrm{n}). \tag{23}$$

Theorem 2. *The concentrated disturbance D satisfies*

$$D(q, \frac{dq}{dt}, \frac{d^2q}{dt^2}) < l_0 + l_1\|q\| + l2\left\|\frac{dq}{dt}\right\|^2 \tag{24}$$

where L_i (i = 0, 1, 2) are the unknown constants.

The tracking error can converge to zero in finite time by selecting sliding mode surface and control rate under the conditions of both Theorem 1 and Theorem 2. Since the reference value is constant and there is no internal disturbance (D = 0), both Theorems 1 and 2 are satisfied.

Based on these, the following Lyapunov function is selected:

$$v_1 = \frac{1}{2}s^2. \tag{25}$$

Because $v_1 > 0$, then taking the derivative of v_1,

$$\frac{dv_1}{dt} = s\frac{ds}{dt} = s(A(x) + B(x)u) = s(-rsign(s) - is) \le 0. \tag{26}$$

After substituting the control law, the derivative of v_1 is less than 0. Therefore, it satisfies the Lyapunov stability series theorem, and the system is stable.

3.3. Observer Design

Given the intricate interplay among the parameters within the PEMFC system, an observer is essential to optimize tracking issues caused by operational uncertainties and disturbances. A sliding mode observer (SMO) feeds back the output estimation error with a nonlinear term specific to sliding mode control, ensuring that the output estimation error tends to zero. Considering the complex coupled nonlinear system of PEMFCs, a SMO has significant advantages over other linear observers in terms of robustness and dynamic response.

Meanwhile, NTSMC will combine with the SMO to form a dual-sliding-surface robust control system. As shown in Figure 7, the SMO anticipates the unknown parameters of the PEMFC in real time and gives estimated parameters to NTSMC, thereby augmenting the control precision.

According to the simplified Equation (9), the second order derivative of e_1 could be described as

$$\frac{d^2e_1}{dt^2} = a_{16}(\frac{d^2x_4}{dt^2} - \frac{d^2x_1}{dt^2} - \frac{d^2x_2}{dt^2}). \tag{27}$$

First, to further simplify the calculation, let

$$\begin{cases} D_1 = {x_1}^2 + x_1x_2 + a_2x_1 \\ D_2 = {x_2}^2 + x_1x_2 + q_2x_2 \\ F_1 = 2x_1 + x_2 + a_2 \\ F_2 = 2x_2 + x_1 + a_2 \end{cases} \tag{28}$$

Then, taking Equation (27) into Equations (19) and (21), $\frac{d^2e_1}{dt^2}$ can be depicted as

$$\begin{aligned}\frac{d^2e_1}{dt^2} &= (a_{14}a_{16}f(x_4) + 2a_1 - \tfrac{a_3a_4a_{20}(D_1+D_2)}{\psi(X)^2} + \tfrac{a_3a_{20}(F_1+x_2)}{\psi(X)})\tfrac{dx_1}{dt} \\ &+ (a_{14}q_{16}f(x_4) + 2a_1 - \tfrac{a_3a_5a_{20}(D_1+D_2)}{\psi(X)^2} + \tfrac{a_3a_{20}(F_2+x_1)}{\psi(X)})\tfrac{dx_2}{dt} \\ &- a_7\dot{I} + a_{14}f(x_4)C\tfrac{\partial C}{\partial x_3}(-a_9x_3 - \tfrac{a_{10}}{x_3}(f(x_4)-1)) + a_{13}a_{14}f(x_4)\tfrac{\partial C}{\partial x_3}u \\ &+ {a_{11}}^{-a_{12}}a_{12}a_{14}a_{15}a_{16}{x_4}^{(a_{12}-1)}(C - a_{16}(x_4 - x_1 - x_2 - a_2) - 2a_1 + f(x_4)(\tfrac{\partial C}{\partial x_4} - a_{16})\tfrac{dx_4}{dt}\end{aligned} \tag{29}$$

where $f(x_4)$ and $\psi(x)$ can be denoted as

$$\begin{cases} f(x_4) = 1 + (a_{15}(\frac{x_4}{a_{11}})^{a_{12}} - 1) \\ \psi(x) = a_4x_1 + a_5x_2 + a_6 \end{cases}.$$

Based on the process of deduction below, Equation (24) could further be described as

$$\frac{d^2e_1}{dt^2} = \alpha_1(X) + \alpha_2(X)u \tag{30}$$

where $\alpha_1(x)$ and $\alpha_2(x)$ can be represented as

$$\begin{cases} \alpha_1(x) = {a_{11}}^{-a_{12}}a_{12}a_{14}a_{15}a_{16}{x_4}^{(a_{12}-1)}(C - a_{16}(x_4 - x_1 - x_2 - a_2) - 2a_1 + f(x_4)(\tfrac{\partial C}{\partial x_4} - a_{16})\tfrac{dx_4}{dt} \\ \quad + (a_{14}a_{16}f(x_4) + 2a_1 - \tfrac{a_3a_4a_{20}(D_1+D_2)}{\psi(x)^2} + \tfrac{a_3a_{20}(F_1+x_2)}{\psi(x)})\tfrac{dx_1}{dt} \\ \quad + (a_{14}a_{16}f(x_4) + 2a_1 - \tfrac{a_3a_5a_{20}(D_1+D_2)}{\psi(x)^2} + \tfrac{a_3a_{20}(F_2+x_1)}{\psi(x)})\tfrac{dx_2}{dt} \\ \quad - a_7\frac{dI_{st}}{dt} + E \\ \alpha_2(x) = a_{13}a_{14}f(x_4)\frac{\partial C}{\partial x_3} \end{cases}$$

where E can be denoted as

$$E = a_{14}f(x_4)C\frac{\partial C}{\partial x_3}(-a_9x_3 - \frac{a_{10}}{x_3}(f(x_4)-1)).$$

Based on these, the system error could be described as

$$\begin{cases} \alpha_1(x) = T\beta_1(x) \\ \frac{d^2e}{dt^2} = T\beta_1(x) + \beta_2(x)u \end{cases}. \tag{31}$$

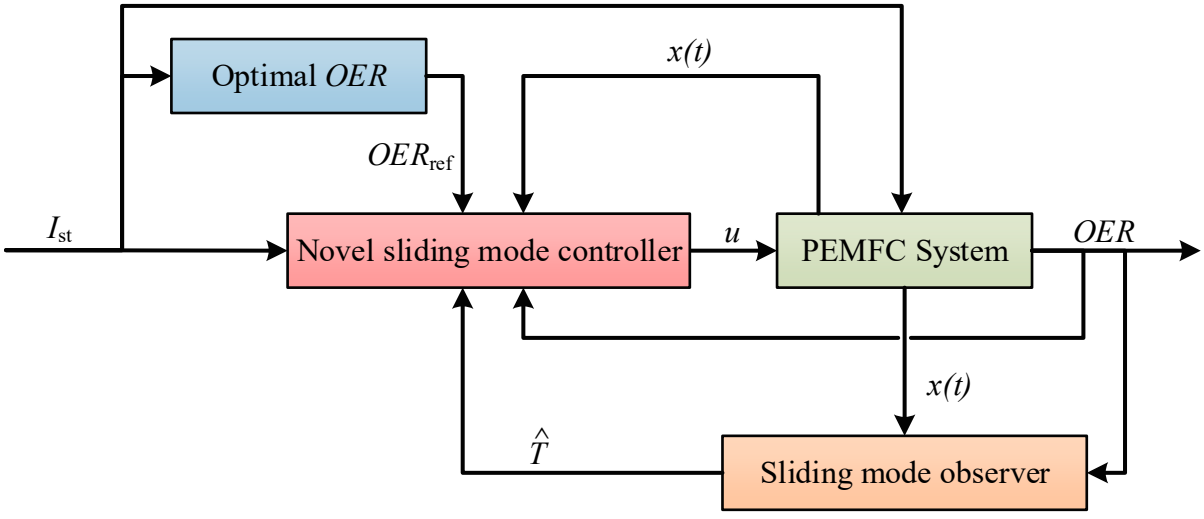


Figure 7. The control block diagram of the complete control system.

As mentioned above, most of the system parameters from a_1 to a_{24} are physical or fixed constants, which can be calculated with physical and equipment parameters, and will not interfere with the normal operation of the system. Among them, a_1, a_3, and a_{20} need to be estimated by the observer. These values are generally obtained by empirical formulas in previous publications. For details, please refer to Appendix A.

In Equation (27), $\zeta_1(x) = (E, \frac{dx_4}{dt}, \frac{dx_1}{dt}, \frac{dx_2}{dt}, \frac{dI_{st}}{dt})$ and $T = (1, T_1, T_2, T_3, T_4)^T$. Since the parameters are difficult to obtain accurately due to disturbance and uncertainty, the sliding variable of the observer is designed as follows:

$$s_1 = \nu_0 e_{tuta} + \nu_1 \frac{de_{tuta}}{dt}. \tag{32}$$

According to Ref. [23], the sliding mode observer is designed as

$$\begin{cases} \frac{d^2 e_{1hat}}{dt^2} = T_{hat}\beta_1(X) + \beta_2(X)u - \frac{ds_0}{dt} - \sigma_0 s_0 + \frac{d^2 e_{1tuta}}{dt^2} \\ \frac{dT_{hat}}{dt} = -\sigma_1 s_0 {\beta_1}^T(X) \end{cases} \tag{33}$$

where estimate values are T_{hat} and e_{1hat}, estimate errors are $T_{tuta} = T - T_{hat}$ and $e_{1tuta} = e_1 - e_{1hat}$, and where σ_0 and σ_1 are gain constants of the sliding mode observer. Let $\nu_1 = 1$, and we can obtain

$$\begin{cases} \frac{d^2 e_{1hat}}{dt^2} = T_{hat}\beta_1(x) + \beta_2(x)u - \nu_0 \frac{de_{1tuta}}{dt} - \sigma_0 s_0 \\ \frac{dT_{hat}}{dt} = -\sigma_1 s_0 {\beta_1}^T(X) \end{cases}. \tag{34}$$

For additional content and specific stability proof please refer to Ref. [28]. Therefore, a new adaptive controller for unknown parameters is obtained by combining the sliding mode observer with the nonsingular terminal sliding mode controller in the previous section.

Firstly, the error obtained by the observer is substituted into system error. Let

$$e_1 = e_{1hat}. \tag{35}$$

Then, the sliding surface s_1 is designed as

$$\begin{cases} s_2 = \frac{de_{1hat}}{dt} + \kappa_1 e_{1hat} + \kappa_2 g(e_{1hat}) \\ g(e_1) = \begin{cases} e_{1hat}^{p1/p2} \text{ if ss} = 0 \text{ or ss} \neq 0, |e_{1hat}| \geq \mu \\ \gamma_1 e_{1hat} + \gamma_2 sign(e_{1hat}) e_{1hat}^2 \text{ if ss} \neq 0, |e_{1hat}| < \mu \end{cases} \end{cases} \tag{36}$$

Finally, according to the Equations (17) to (22), the new control input u can be solved as

$$\begin{cases} u = \frac{1}{b(x)}(-rsign(s_2) - is_2 - a(x)) \\ \begin{cases} a(x) = -a_{16}(\frac{d^2 x_1}{dt^2} + \frac{d^2 x_2}{dt^2}) + a_{16}(\frac{dx_4}{dt}\frac{\partial}{\partial x_4}(\frac{dx_4}{dt}) + \frac{dx_1}{dt}\frac{\partial}{\partial x_1}(\frac{dx_4}{dt}) + \frac{dx_2}{dt}\frac{\partial}{\partial x_2}(\frac{dx_4}{dt})) \\ \qquad + a_{16}\frac{\partial}{\partial x_3}(\frac{dx_4}{dt})(-a_9 x_3 - \frac{a_{10}}{x_3}((\frac{x_4}{a_{14}})^{a_{12}} - 1))C + \kappa_1 \frac{dg(e_{1\text{hat}})}{dt} \\ \mathrm{b}(x) = a_{13}a_{16}\frac{\partial}{\partial x_3}(\frac{dx_4}{dt}) \end{cases} \end{cases} \tag{37}$$

4. Results and Discussion

4.1. Simulation Verification Under Simple Step Signals

A variable electric current input is given to the system as shown in Figure 8. In order to verify the performance, efficiency, and robustness of the proposed control strategy, the detailed simulation is divided into the following three parts. They are error analysis, control target analysis, and comparison. In Appendix A, the operating parameters for the simulation are collected and illustrated. Since the given current is dynamic, the set value of the optimal OER of the control target also has a dynamic range.

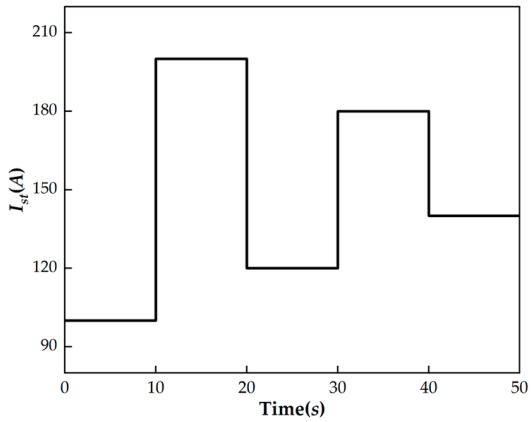


Figure 8. The input electric current of the PEMFC system.

Figure 8 illustrates periodic step changes in the operating current over a 50 s interval. The sequence is as follows: the current starts at 100 A for the first 10 s interval, jumps to 200 A for the second 10 s interval, then reduces to 120 A until 30 s. It then increases to 180 A, continuing until 40 s, after which it drops to 140 A for the final 10 s.

Figure 9a–d displays the estimates derived from the sliding mode observer, as previously designed. The observer's ability to accurately estimate the state parameters in response to current dynamics is evident from the figure. Consequently, the implementation of this observer ensures more precise estimations of these unknown parameters.

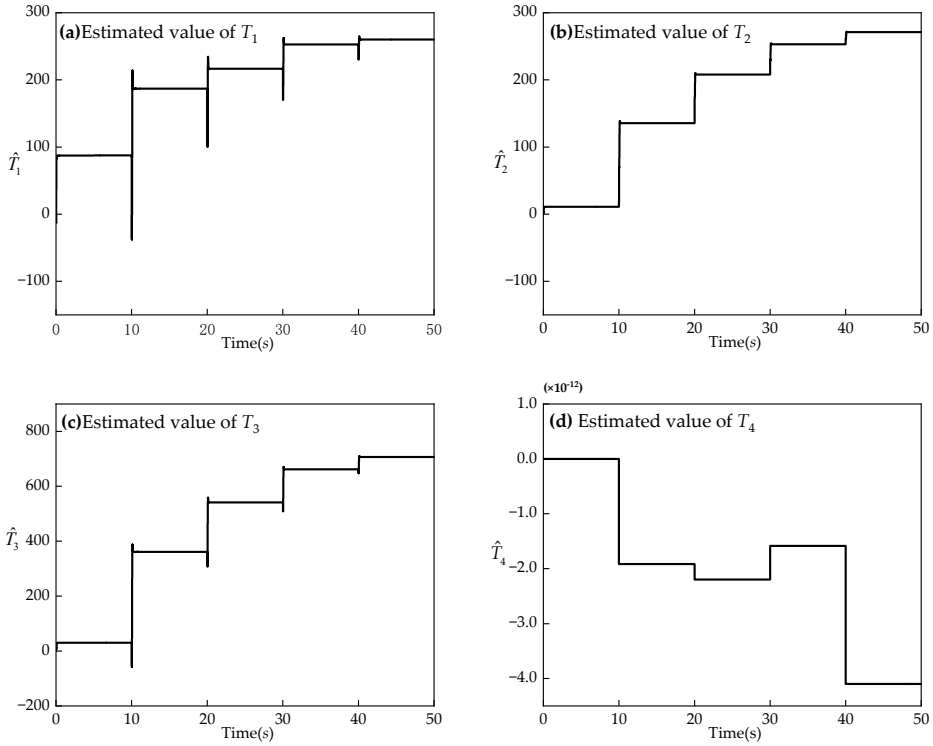


Figure 9. Estimate values of observer.

Figure 10b shows the variation of the new controller sliding variable over time. This parameter shows that the controller is always able to stabilize the system by guiding it towards its origin along the switching surface. From the OER results, even if there is a overshoot on the sliding surface, it does not negatively affect the control objective. Like the previous error and OER plots, the sliding surface graphically confirms that the system achieves zero delay and finite time convergence. Figure 10a depicts the sliding surface formed by the sliding mode observer.

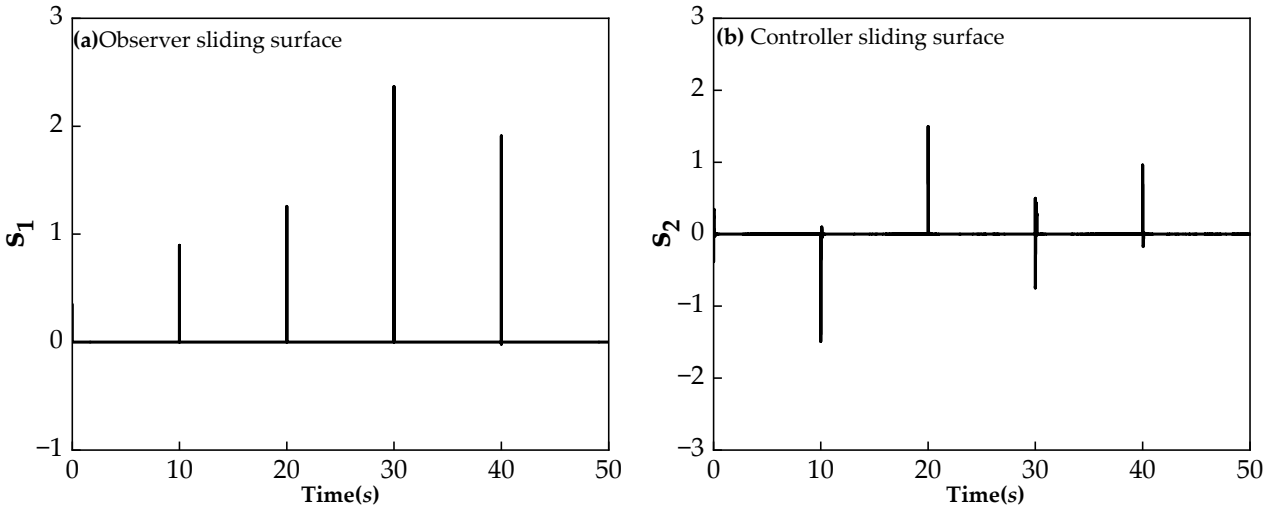


Figure 10. Observer sliding surface and controller sliding surface.

Figure 11 displays the compressor input voltage in relation to changes in stack current. Specifically, the voltage increases at the 10th and 30th seconds, coinciding with rises in stack current, and decreases at the 20th and 40th seconds as the stack current drops. During stable current periods, such as from 10 to 20 s and 20 to 30 s, the controller stabilizes the compressor input voltage. The observed consistency between the compressor voltage variations and the stack current changes confirms that the control strategy effectively achieves satisfactory tracking regulation.

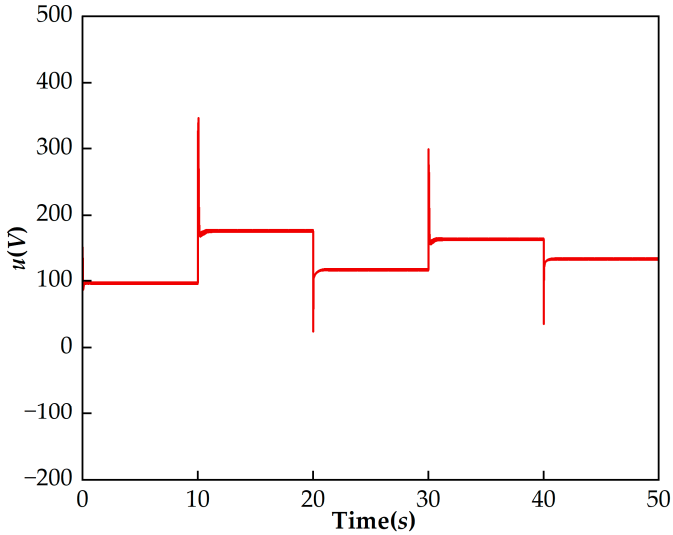


Figure 11. Compressor voltage.

Figures 12a,b illustrate the output voltage and net output power of the PEMFC stack system, respectively. The net output power is defined as the disparity between the stack's output power and the power consumed by the subsystem, specifically the compressor. As evident from the figures, both the output voltage and net power exhibit a rapid response to abrupt alterations in current, achieving a steady state promptly. An average delay of approximately 0.8 s is observed, attributable to the electrochemical dynamics of the PEMFC stack. Furthermore, the lower overshoot indirectly signifies the robust nature of the control system implemented.

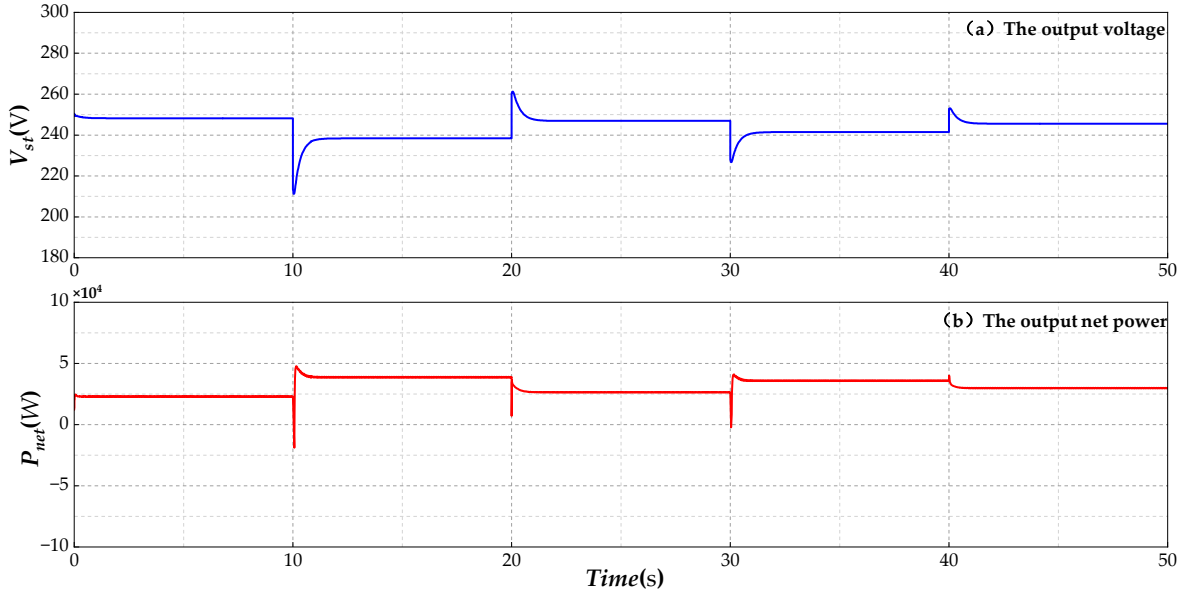


Figure 12. The output voltage of the PEMFC system and the net output power.

The operating parameters and input stack currents of the newly developed controller exhibit consistency with those of the existing controllers. In Figure 13, the OER tracking curve for the novel sliding mode controller is represented by the red line, while the TSMC and SMC are depicted by the blue and grey lines, respectively. Detailed conditions of each current transition are provided in subfigures (A) through (D). Notably, the novel controller demonstrates rapid convergence within a finite timeframe and boasts the fastest tracking performance among the compared systems according to Table 2. This swift response time enables the PEMFC to swiftly attain its optimal output state, thereby enhancing its overall efficiency. This improvement is attributable to the optimized sliding mode structure incorporated into the new controller, which surpasses the asymptotic stability achieved by traditional SMC. Furthermore, although the new controller exhibits a slight overshoot compared to the TSMC, its OER tracking performance underscores its enhanced capability in effectively managing dynamic conditions.

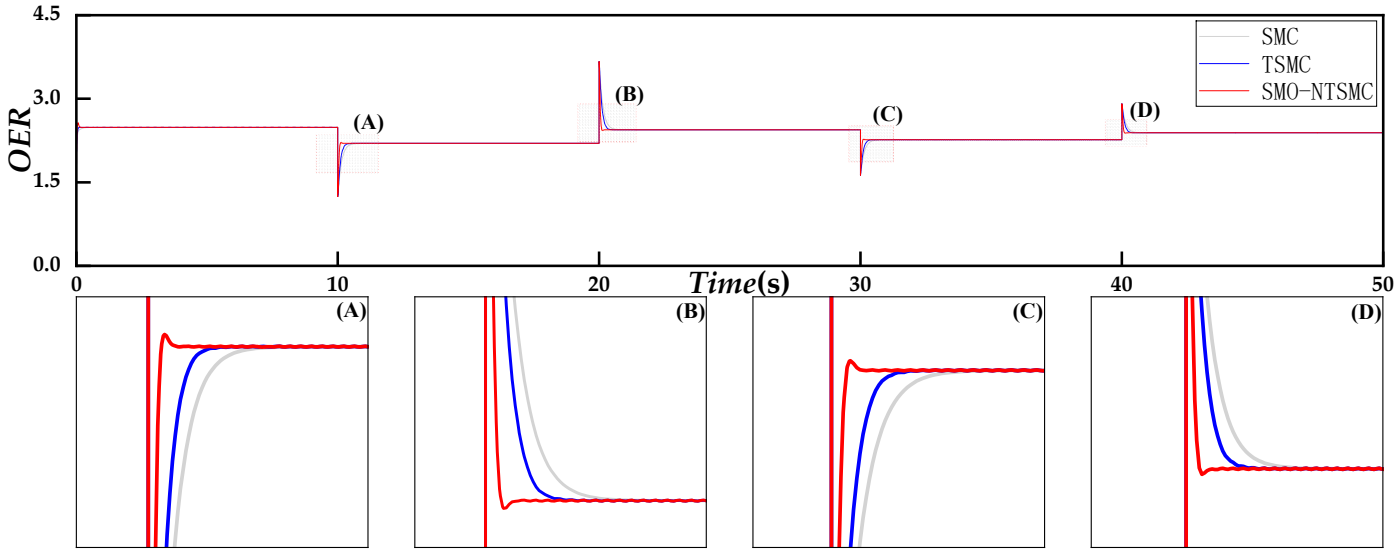


Figure 13. OER.

Table 2. Tracking performance comparisons.

Controller	Start-Up Time	Rising Time	Overshoot
SMC	0.72 s	0.71 s	100%
TSMC	0.37 s	0.33 s	103%
SMO-NTSMC	0.14 s	0.08 s	98%

The error curve of the PEMFC system is illustrated in Figure 14, and a comparison of error performance between different controllers is summarized in Table 3. Upon examination of the figure, it is evident that all controllers exhibit minimal steady-state error during steady-state operation. However, a detailed analysis of subplots (A) to (D) reveals that the conventional sliding mode controller experiences a response delay of approximately 0.8 s, whereas the TSMC exhibits a delay of 0.45 s in response to abrupt current changes. In contrast, the novel sliding mode controller demonstrates superior convergence in its response. Specifically, its response speed is enhanced by 63% when compared to the TSMC. Additionally, the new controller exhibits the lowest overshoot, highlighting its exceptional robustness. This enhanced performance is attributed to the further optimization of the sliding mode structure within the terminal sliding mode controller, coupled with the incorporation of a sliding mode observer that significantly improves the controller's accuracy and system stability.

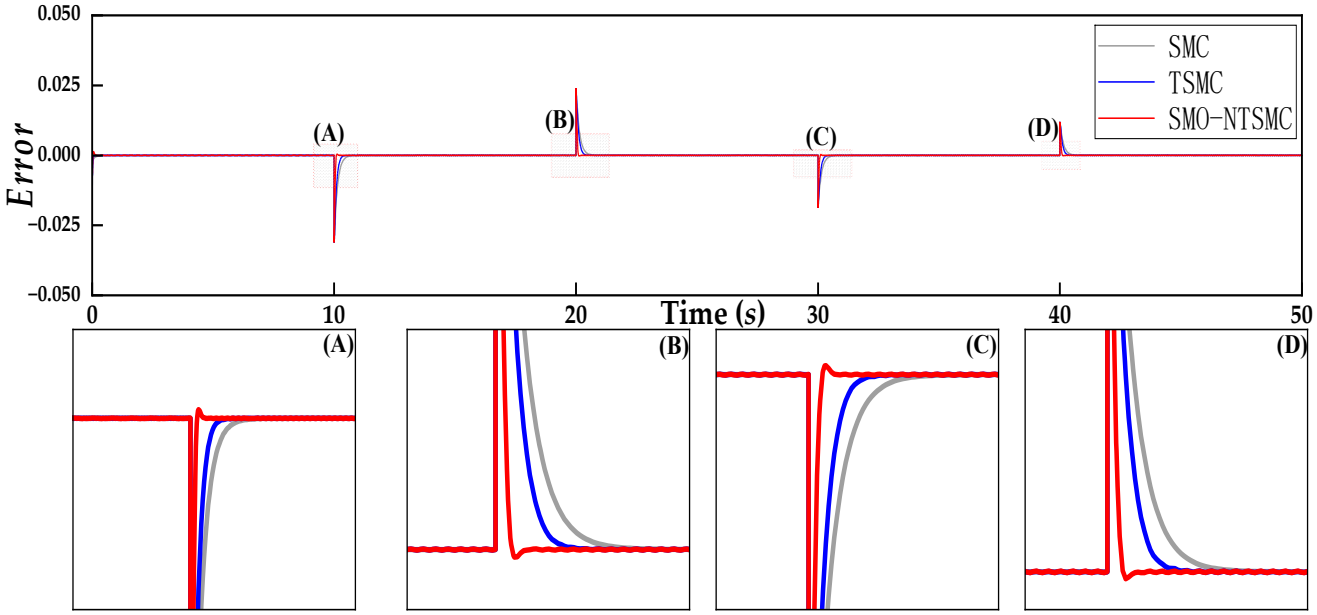


Figure 14. System tracking error.

Table 3. Error results comparisons.

Controller	Average Respond Delay	Max Error	Average Overshoot
SMC	0.80 s	0.029	100%
TSMC	0.45 s	0.026	104%
SMO-NTSMC	0.17 s	0.025	96%

Figure 15 shows the changes of some state parameters with time. They are the cathode oxygen pressure, cathode nitrogen pressure, cathode pressure, compressor motor speed, and supply manifold pressure. These five figures show that the four parameters and *Pca* change accurately with the change of the stack electric current, and indirectly prove the response of the control objective.

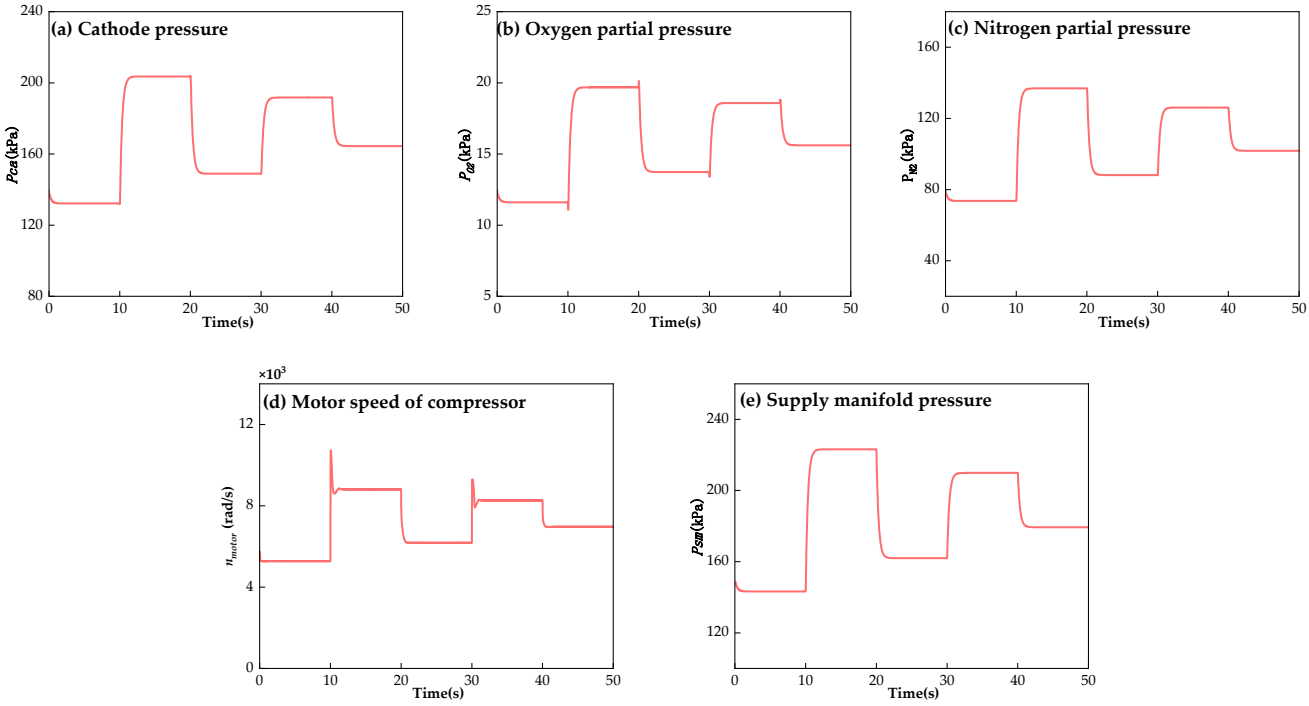


Figure 15. State parameters.

4.2. Simulation Verification Under Step Signals with Noise Interference

To better simulate real experimental conditions, we incorporated external ambient noise into our analysis. Additionally, to assess the controller's performance under prolonged noise, we extended the duration of each current interval. Specifically, as shown in Figure 16, we adjusted the original step change from 10 s to 20 s.

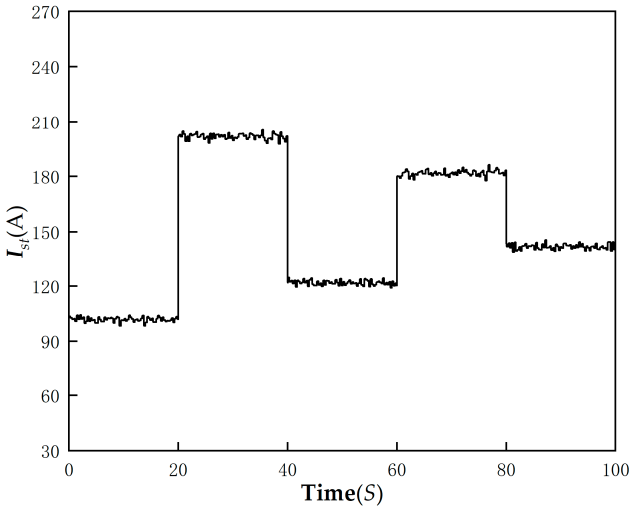


Figure 16. Input current of the PEMFC system (with noise interference).

The operating parameters and input noise stack currents of the newly designed controller align with those of the other controllers. In Figure 17, which depicts the time-varying OER, it is evident that the new controller has the strongest tracking performance and robustness, as in the steady state. From the subplots (A–D), the designed controller exhibits superior capability in noise suppression. In contrast, the noise disturbances observed in all other controllers displayed increased fluctuations and more significant deviations.

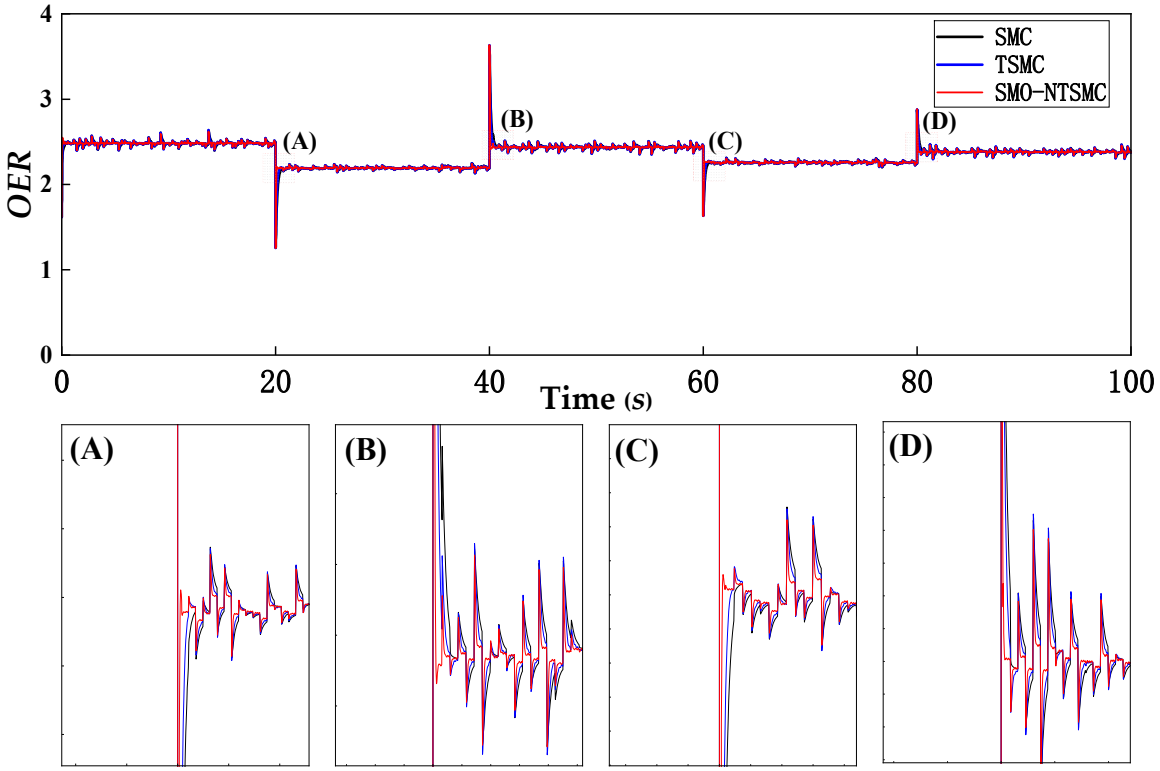


Figure 17. OER (with noise interference).

5. Conclusions

In this paper, we introduced an innovative control methodology aimed at optimizing the air-feeding of PEMFCs. The principal results derived from our study are summarized as below:

(i) Our proposed controller exhibits finite-time convergence, which is much better than the conventional sliding mode controller that can only achieve asymptotic stability. The performance improvement is 63% compared to TSMC, and several times that of SMC.

(ii) Owing to its superior robustness and resilience to interference, the novel controller outperforms other controllers in critical performance indicators, particularly in response to abrupt changes and noise rejection. These advantages are attributed to the incorporation of a new sliding mode structure and an observer with a more robust sliding mode surface than conventional approaches.

(iii) The integration of observers allows the system to adapt to unknown parameters, thereby enhancing efficiency and accuracy. Furthermore, the controller's dual sliding mode surface structure reinforces the system's robustness.

(iv) In summary, the proposed advanced air management technique tailored for PEMFCs enhances tracking performance and response speed by over 70% compared to existing methodologies. The reduction in overshoot and the improvement in system stability contribute to the PEMFC's efficiency, while the robust noise suppression capability minimizes disturbances.

In our future research endeavors, we plan to apply this methodology to automotive fuel cell systems, where further experimental studies will be conducted to optimize power output even further.

Author Contributions: Methodology, S.F.; Validation, S.F., J.F. and D.C.; Formal analysis, S.F.; Investigation, X.F.; Resources, S.F. and C.T.; Data curation, S.F. and J.F.; Writing—original draft, S.F.; Writing—review & editing, S.F., J.F., X.F. and D.C.; Supervision, J.F., X.F., D.C. and C.T.; Project administration, X.F.; Funding acquisition, X.F. All authors have read and agreed to the published version of the manuscript.

Funding: This research received no external funding. The APC was funded by [National Natural Science Foundation of China] grant number [22179054].

Data Availability Statement: The original contributions presented in this study are included in the article.

Acknowledgments: We gratefully acknowledge the financial support from the National Natural Science Foundation of China (52205271 and 22179054), Ministry of Science and Technology of the People's Republic of China (G2022014065L), and the Innovation Support Program of Science and Technology Program of Jiangsu Province (SBZ2023080107).

Conflicts of Interest: The authors declare no conflicts of interest.

Appendix A

The internal and auxiliary system parameters of the PEMFC system, denoted as a_i for i = 1, . . ., 24 in the state equations, are described as

$$a_1 = \frac{RT_{st}k_{ca,in}}{M_{O2}V_{ca}}\left(\frac{\chi_{O_2,atm}}{1+\omega_{atm}}\right),\ a_2 = P_{sat},\ a_3 = \frac{RT_{st}}{V_{ca}},\ a_4 = M_{O_2},\ a_5 = M_{N_2},\ a_6 = M_V P_{sat},$$
$$a_7 = \frac{RT_{st}n}{4FV_{ca}},\ a_8 = \frac{RT_{st}k_{ca,in}}{M_{N2}V_{ca}}\left(\frac{1-\chi_{O_2,atm}}{1+\omega_{atm}}\right),\ a_9 = \frac{k_t k_v \eta_{cm}}{R_{cm}J_{cp}},\ a_{10} = \frac{T_{atm}C_p}{J_{cp}\eta_{cp}},\ a_{11} = P_{atm},$$
$$a_{12} = \frac{\gamma-1}{\gamma},\ a_{13} = \frac{k_t\eta_{cm}}{R_{cm}J_{cp}},\ a_{14} = \frac{RT_{atm}\gamma}{M_{atm}V_{sm}},\ a_{15} = \frac{1}{\eta_{cp}},\ a_{16} = k_{ca,in},\ a_{17} = \frac{A_T C_D}{\sqrt{RT_{st}}}\sqrt{\frac{2\gamma}{\gamma-1}},$$
$$a_{18} = \frac{1}{\gamma},\ a_{19} = \left(\frac{2}{\gamma+1}\right)^{\frac{\gamma}{\gamma-1}},\ a_{20} = \frac{A_T C_D}{\sqrt{RT_{st}}}\gamma^{0.5}\left(\frac{2}{\gamma+1}\right)^{\frac{\gamma+1}{2\gamma-1}},\ a_{21} = \frac{1}{R_{cm}},\ a_{22} = k_v,$$
$$a_{23} = \frac{X_{O_2,atm}}{1+\omega_{atm}},\ a_{24} = \frac{nM_{O_2}}{4F}$$

where the relevant parameters in the above formulas are included in Table 1.

References

1. Gao, X.; An, R. Research on the Coordinated Development Capacity of China's Hydrogen Energy Industry Chain. *J. Clean. Prod.* **2022**, *377*, 134177. [CrossRef]
2. Chen, L.; Ma, R. Clean Energy Synergy with Electric Vehicles: Insights into Carbon Footprint. *Energy Strategy Rev.* **2024**, *53*, 101394. [CrossRef]
3. Zou, T.; Guo, P.; Li, F.; Wu, Q. Research Topic Identification and Trend Prediction of China's Energy Policy: A Combined LDA-ARIMA Approach. *Renew. Energy* **2024**, *220*, 119619. [CrossRef]
4. Jiang, B.; Raza, M.Y. Research on China's Renewable Energy Policies under the Dual Carbon Goals: A Political Discourse Analysis. *Energy Strategy Rev.* **2023**, *48*, 101118. [CrossRef]
5. Hu, D.; Wang, Y.; Li, J.; Yang, Q.; Wang, J. Investigation of Optimal Operating Temperature for the PEMFC and Its Tracking Control for Energy Saving in Vehicle Applications. *Energy Convers. Manag.* **2021**, *249*, 114842. [CrossRef]
6. Salam, M.A.; Shaikh, M.A.A.; Ahmed, K. Green Hydrogen Based Power Generation Prospect for Sustainable Development of Bangladesh Using PEMFC and Hydrogen Gas Turbine. *Energy Rep.* **2023**, *9*, 3406–3416. [CrossRef]
7. Xiao, C.; Wang, B.; Wang, C.; Yan, Y. Design of a Novel Fully-Active PEMFC-Lithium Battery Hybrid Power System Based on Two Automatic ON/OFF Switches for Unmanned Aerial Vehicle Applications. *Energy Convers. Manag.* **2023**, *292*, 117417. [CrossRef]
8. Shahverdian, M.H.; Sohani, A.; Pedram, M.Z.; Sayyaadi, H. An Optimal Strategy for Application of Photovoltaic-Wind Turbine with PEMEC-PEMFC Hydrogen Storage System Based on Techno-Economic, Environmental, and Availability Indicators. *J. Clean. Prod.* **2023**, *384*, 135499. [CrossRef]
9. Chen, D.; Xu, Y.; Tade, M.O.; Shao, Z. General Regulation of Air Flow Distribution Characteristics within Planar Solid Oxide Fuel Cell Stacks. *ACS Energy Lett.* **2017**, *2*, 319–326. [CrossRef]
10. Qian, P.; Liu, L.; Pu, C.; Meng, D.; Páez, L.M.R. Methods to Improve Motion Servo Control Accuracy of Pneumatic Cylinders—Review and Prospect. *Int. J. Hydromechatronics* **2023**, *6*, 274–310. [CrossRef]
11. Wang, Y.; Wang, Y. Pressure and Oxygen Excess Ratio Control of PEMFC Air Management System Based on Neural Network and Prescribed Performance. *Eng. Appl. Artif. Intell.* **2023**, *121*, 105850. [CrossRef]
12. Jung, S.Y.; Nguyen, T.V. An Along-the-Channel Model for Proton Exchange Membrane Fuel Cells. *J. Electrochem. Soc.* **1998**, *145*, 1149.

13. Wang, F.-C.; Yang, Y.-P.; Huang, C.-W.; Chang, H.-P.; Chen, H.-T. System Identification and Robust Control of a Portable Proton Exchange Membrane Full-Cell System. *J. Power Sources* **2007**, *164*, 704–712. [CrossRef]
14. Fathollahi, A.; Gheisarnejad, M.; Andresen, B.; Farsizadeh, H.; Khooban, M.-H. Robust Artificial Intelligence Controller for Stabilization of Full-Bridge Converters Feeding Constant Power Loads. *IEEE Trans. Circuits Syst. II Express Briefs* **2023**, *70*, 3504–3508. [CrossRef]
15. Baroud, Z.; Benmiloud, M.; Benalia, A.; Ocampo-Martinez, C. Novel Hybrid Fuzzy-PID Control Scheme for Air Supply in PEM Fuel-Cell-Based Systems. *Int. J. Hydrogen Energy* **2017**, *42*, 10435–10447. [CrossRef]
16. Zhao, D.; Li, F.; Ma, R.; Zhao, G.; Huangfu, Y. An Unknown Input Nonlinear Observer Based Fractional Order PID Control of Fuel Cell Air Supply System. *IEEE Trans. Ind. Appl.* **2020**, *56*, 5523–5532. [CrossRef]
17. Yue, H.; He, H.; Han, M.; Gong, S. Active Disturbance Rejection Control Strategy for PEMFC Oxygen Excess Ratio Based on Adaptive Internal State Estimation Using Unscented Kalman Filter. *Fuel* **2024**, *356*, 129619. [CrossRef]
18. Lu, Y.; Tan, C.; Ge, W.; Li, B.; Lu, J. Improved Sliding Mode-Active Disturbance Rejection Control of Electromagnetic Linear Actuator for Direct-Drive System. *Actuators* **2021**, *10*, 138. [CrossRef]
19. Tan, C.; Ren, H.; Li, B.; Lu, J.; Li, D.; Tao, W. Design and Analysis of a Novel Cascade Control Algorithm for Braking-by-Wire System Based on Electromagnetic Direct-Drive Valves. *J. Frankl. Inst.* **2022**, *359*, 8497–8521. [CrossRef]
20. Aykut Korkmaz, S.; Ayten Çetinkaya, S.; Yuksel, O.; Konur, O.; Emrah Erginer, K.; Ozgur Colpan, C. Fixed Time Adaptive Fault Tolerant Sliding Mode Control of PEMFC Air Supply System. *Int. J. Hydrogen Energy* **2024**, *51*, 1402–1420. [CrossRef]
21. Silaa, M.Y.; Bencherif, A.; Barambones, O. A Novel Robust Adaptive Sliding Mode Control Using Stochastic Gradient Descent for PEMFC Power System. *Int. J. Hydrogen Energy* **2023**, *48*, 17277–17292. [CrossRef]
22. Abbaker, A.M.O.; Wang, H.; Tian, Y. Adaptive Integral Type-terminal Sliding Mode Control for PEMFC Air Supply System Using Time Delay Estimation Algorithm. *Asian J. Control* **2022**, *24*, 217–226. [CrossRef]
23. Fang, S.; Zhang, R.; Maltsev, S.; Chen, D.; Fan, X.; Levtsev, A. A Novel Adaptive Fast Sliding Mode Control Method Based on Fuzzy Algorithm for the Air Management System of Fuel Cell Stack. *Process Saf. Environ. Prot.* **2024**, *187*, 506–517. [CrossRef]
24. Liu, Z.; Chang, G.; Yuan, H.; Tang, W.; Xie, J.; Wei, X.; Dai, H. Adaptive Look-Ahead Model Predictive Control Strategy of Vehicular PEMFC Thermal Management. *Energy* **2023**, *285*, 129176. [CrossRef]
25. Yang, D.; Pan, R.; Wang, Y.; Chen, Z. Modeling and Control of PEMFC Air Supply System Based on T-S Fuzzy Theory and Predictive Control. *Energy* **2019**, *188*, 116078. [CrossRef]
26. Wang, Y.; Li, H.; Feng, H.; Han, K.; He, S.; Gao, M. Simulation Study on the PEMFC Oxygen Starvation Based on the Coupling Algorithm of Model Predictive Control and PID. *Energy Convers. Manag.* **2021**, *249*, 114851. [CrossRef]
27. Huo, W.; Li, W.; Zhang, Z.; Sun, C.; Zhou, F.; Gong, G. Performance Prediction of Proton-Exchange Membrane Fuel Cell Based on Convolutional Neural Network and Random Forest Feature Selection. *Energy Convers. Manag.* **2021**, *243*, 114367. [CrossRef]
28. Zhu, Y.; Zou, J.; Li, S.; Peng, C. An Adaptive Sliding Mode Observer Based Near-Optimal OER Tracking Control Approach for PEMFC under Dynamic Operation Condition. *Int. J. Hydrogen Energy* **2022**, *47*, 1157–1171. [CrossRef]
29. Feng, Y.; Yu, X.; Man, Z. Non-Singular Terminal Sliding Mode Control of Rigid Manipulators. *Automatica* **2002**, *38*, 2159–2167. [CrossRef]
30. Pukrushpan, J.T. Modeling and Control of PEM Fuel Cell Systems and Fuel Processors. Ph.D. Dissertation, University of Michigan, Ann Arbor, MI, USA, 2003.
31. Chen, X.; Fang, Y.; Liu, Q.; He, L.; Zhao, Y.; Huang, T.; Wan, Z.; Wang, X. Temperature and Voltage Dynamic Control of PEMFC Stack Using MPC Method. *Energy Rep.* **2022**, *8*, 798–808. [CrossRef]
32. Yang, Y.; Bai, M.; Zhou, Z.; Wu, W.-T.; Zhao, J.; Wei, L.; Li, Y.; Li, Y.; Song, Y. A 3D PtCo Degradation Model for Long-Term Performance Prediction of a Scaled-up PEMFC under Constant Voltage Operation. *Energy Convers. Manag.* **2024**, *300*, 117918. [CrossRef]
33. Wang, Y.; Wang, C.-Y. Dynamics of Polymer Electrolyte Fuel Cells Undergoing Load Changes. *Electrochim. Acta* **2006**, *51*, 3924–3933. [CrossRef]
34. Gruber, J.K.; Bordons, C.; Dorado, F. Nonlinear Control of the Air Feed of a Fuel Cell. In Proceedings of the 2008 American Control Conference, Seattle, WA, USA, 11–13 June 2008; IEEE: Piscataway, NJ, USA, 2008; pp. 1121–1126.
35. Fathollahi, A.; Andresen, B. Adaptive Fixed-Time Control Strategy of Generator Excitation and Thyristor-Controlled Series Capacitor in Multi-Machine Energy Systems. *IEEE Access* **2024**, *12*, 100316–100327. [CrossRef]

Disclaimer/Publisher's Note: The statements, opinions and data contained in all publications are solely those of the individual author(s) and contributor(s) and not of MDPI and/or the editor(s). MDPI and/or the editor(s) disclaim responsibility for any injury to people or property resulting from any ideas, methods, instructions or products referred to in the content.